Nonlinear Elastic Wave Tomography for the Imaging of Corrosion Damage

Francesco Ciampa[1], Gennaro Scarselli[2], Simon Pickering[1], M. Meo[1*]

[1]Department of Mechanical Engineering, University of Bath, Bath BA2 7AY, UK

[2]Department of Engineering for Innovation, University of Salento, Via per Monteroni (Lecce), 73100, Italy

Abstract

This paper presents a nonlinear elastic wave tomography method, based on ultrasonic guided waves, for the image of nonlinear signatures in the dynamic response of a damaged isotropic structure. The proposed technique relies on a combination of high order statistics and a radial basis function approach. The bicoherence of ultrasonic waveforms originated by a harmonic excitation was used to characterise the second order nonlinear signature contained in the measured signals due to the presence of surface corrosion. Then, a radial basis function interpolation was employed to achieve an effective visualization of the damage over the panel using only a limited number of receiver sensors. The robustness of the proposed nonlinear imaging method was experimentally demonstrated on a damaged 2024 aluminium panel, and the nonlinear source location was detected with a high level of accuracy, even with few receiving elements. Compared to five standard ultrasonic imaging methods, this nonlinear tomography technique does not require any baseline with the undamaged structure for

* Corresponding author: m.meo@bath.ac.uk

the evaluation of the corrosion damage, nor a priori knowledge of the mechanical properties of the specimen.

Keywords: nonlinear imaging methods, structural health monitoring, ultrasonic guided waves, bispectral analysis.

I. Introduction

Structural health monitoring imaging systems based on ultrasonic guided waves are used to detect and assess material damages in isotropic and composite structures and can be classified in linear (LUIM) and nonlinear (NUIM) ultrasonic imaging methods. Both approaches are based on generating stress waves within the structure using a finite number of surface bonded piezoelectric transmitters, and then, the elastic wave response is recorded by a sparse array of receiver sensors. LUIM rely on linear elastodynamic theory and measure the reflection and scattering of primary waves at the material heterogeneities and discontinuities (e.g. wave speed, damping variations, etc…). The presence of defects changes the phase and amplitude of the measured signals, but the frequency of the input waveforms is unchanged [1] [2]. Indeed, LUIM such as elliptical [3], hyperbolic [4], energy arrival [5] and the Reconstruction Algorithm for the Probabilistic Inspection Damage (RAPID) [6] are quite advanced and mature and provide a detailed image of the structural damage. Rayleigh Maximum Likelihood Estimation (RMLE) method is another linear imaging technique able to locate structural defects using guided waves to feed a Rayleigh based statistical model of scattered wave measurements [7]. However, the major drawback of these imaging methods is that a baseline (i.e. a representation of the undamaged structure) is needed as well as a known group velocity of the propagating elastic waves. Moreover, LUIM are able to detect and localise the damage only in the presence of a significant impedance contrast. However,

when the impedance mismatch is less pronounced, a micro-damage is present in the form of a nonlinear elastic zone within the medium. In other words, LUIM may not detect small defect before they grow to a critical size of few millimetres, as the contribution on the total structural stiffness and the elastic scattering from flaws originating at incipient stages of damage development (e.g. micro-cracks) is negligible. Nonlinear elastic effects of damaged materials such as higher and sub-harmonics generation can be assessed with both numerical multiscale materials models [8], [9], [10] and experimental nonlinear elastic wave spectroscopy (NEWS) methods [11], [12], [13]. Particularly, NEWS techniques measure nonlinear classical and non-classical phenomena in the kHz and MHz range and they have shown an extreme sensitivity in diagnosing manufacturing defects such as porosity, undesired component assembly contact conditions, and incipient damage in the form of micro-cracks, delaminations, clapping areas, adhesive bond weakening, etc… [14]. Based on these considerations, NUIM are the most promising imaging techniques in terms of reliability, accuracy and ease of implementation, and they can be distinguished in nonlinear inverse filtering (NIF) and nonlinear elastic wave tomography (NEWT) methods. NIF associated with NEWS and phase symmetry analysis with chirp excitation signals can be used to retrieve the optimal refocusing at the nonlinear scatterer location due to the presence of structural flaws [15]. This baseline-free imaging technique can be used to characterise the nonlinear elastic behaviour of geometrically complex structures and its effects on the wave propagation caused by the presence of defects, even at their early stages. NEWT is a novel nonlinear imaging method that can be used to assess and localise the nonlinear signature in metallic and composite structures. Ciampa et al. [16] presented a NEWT method based on a combination of higher order statistic (HOS) such as

bicoherence analysis and radial basis function (RBF) interpolation in order to image the presence of structural defects on a damaged carbon fibre composite laminate. The aim of this paper is to compare the performance of NEWT with that of five LUIM for the estimation of the damage on an aluminium panel undergone to corrosion. The experimental results showed the effectiveness of the nonlinear tomography sensing technique for structural health monitoring applications as it allowed achieving a perfect localisation of the damage using a reduced number of sparse sensor arrays. Sections II and III describe the principles of NEWT and LUIM adopted in this work. Section IV reports the experimental set-up, whilst Section V illustrates the imaging results of the damage location using both linear and nonlinear imaging methods with a reduced number of receiving elements. Then, the conclusions of this research work are presented.

II. Nonlinear Elastic Wave Tomography

This Section presents the NEWT imaging method developed for evaluating the corrosion damage on an aluminium panel subjected to harmonic excitation. A number of nonlinear parameters have been widely used to detect the presence of cracks and delaminations in both metallic and composite structures, such as the standard second and third order nonlinear coefficients [17], [18], acoustic moments [19], bispectrum [20], [21], cross-modulation coefficients [22], etc… In this work, both the classical second order nonlinear parameter β and the bicoherence b^2 were combined with RBF in order to detect the second order nonlinear elastic response of the medium under wideband excitation using a sparse array of sensing elements. In particular, for the execution of NEWT, M piezoelectric sensors were surface bonded over the top of the

aluminium structure with each transducer serving as both transmitter and receiver. In this manner, M matrices composed by $N = M - 1$ columns and Ξ rows that contained the nonlinear material responses $f_{mn}[\theta]$ with $\theta = 1,\ldots,\Xi$, were generated. Here, m $(1 \le m \le M)$ and n $(1 \le n \le N)$ are the indices associated to the transmitter and receiver transducers, respectively, which are located at coordinates $\mathbf{r}_i = x_i\hat{i} + y_i\hat{j}$ on the top surface of the panel. According to Landau's nonlinear classical theory [23], the nonlinear anharmonic coefficient β_{mn} from each pair of transmitter-receiver sensors can be obtained as a solution of the nonlinear elastodynamic wave equation via a first order perturbation theory as follows:

$$\beta_{mn} \propto \frac{\sqrt{|P_{mn}(\omega_2)|}}{|P_{mn}(\omega_1)|}, \tag{1}$$

where $|P_{mn}(\omega_2)|$ is the magnitude of the power spectral density associated with the second harmonic frequency component measured from each receiver transducer. However, power spectral analysis has the limitation of discarding all phase information contained in the measured signals. Hence, HOS such as bispectral analysis can be used to measure the coupling between the angular frequencies ω_1 and $\omega_2 = 2\omega_1$, i.e. between the fundamental and the second harmonic frequencies. Bispectrum is defined as the two-dimensional Fourier transform of the third order correlation function and it is generally complex valued [24]. For a real, zero-mean stationary waveform $f_{mn}[\theta]$ containing the information of the structural damage, the bicoherence b_{mn}^2 is a useful normalised form of bispectrum that measures the quadratic phase coupling (QPC) on an absolute scale between zero and one [25]. QPC resulting from the nonlinear response of the structure can be used to discriminate between material nonlinear features that would

be quadratic phase coupled and experimental/environmental noise sources that, instead, would not be. Hence, the bicoherence coefficient can be defined as [26]

$$b_{mn}^2 = \frac{|B_{mn}(\omega_1, \omega_1)|^2}{P_{mn}(\omega_1)P_{mn}(\omega_1)P_{mn}(\omega_2)}, \quad (2)$$

with

$$B_{mn}(\omega_1, \omega_1) = E\left[F_{mn}(\omega_1)F_{mn}(\omega_1)F_{mn}^*(\omega_2)\right], \quad (3)$$

where $E[\cdot]$ is the statistical expectation operator of the third order auto-correlation function of the measured waveform, $f_{mn}[\theta]$, $F_{mn}(\omega)$ is the Fourier Transform of $f_{mn}[\theta]$, and the asterisk sign "*" corresponds to a complex conjugate operation. Since the bispectrum has a variance proportional to the triple product of the power spectra, it can result in the second order properties of the measured signal dominating the estimation. The advantage of normalisation is to make the variance approximately flat across all frequencies. Hence, both parameters β_{mn} and b_{mn}^2 were used to characterise the nonlinearity of the structural response. According to the theoretical aspects detailed in [27], a RBF approach was employed to generate the NEWT images of the damage location. The second order nonlinear parameters β_{mn} and b_{mn}^2 were initially evaluated from the waveforms recorded by the *n*th receiver and sent by the *m*th transmitter. The physical intuition behind this is that if a flaw is present on a structure excited at the fundamental angular frequency, ω_1, the values of β_{mn} and b_{mn}^2 estimated from the signals measured by the *N* receivers will be higher in points of the structure close the damage location, $\mathbf{r}_d$, with $\mathbf{r}_d = x_d\hat{i} + y_d\hat{j}$. Then, using the thin plate spline basis function, the nonlinear values in all the coordinates $\mathbf{r} = x\hat{i} + y\hat{j}$ of the aluminium panel were obtained by solving a linear system, whose RBF coefficients were the only

unknown to be calculated [28]. As a result, this procedure led to the creation of M two-dimensional (2D) maps $S_{mn}^{\beta(k)}(\mathbf{r})$ and $S_{mn}^{b^2(k)}(\mathbf{r})$, with $1 \le k \le M$. From these M maps, two final NEWT images $I_{mn}^{\beta}(\mathbf{r})$ and $I_{mn}^{b^2}(\mathbf{r})$ for both coefficients β_{mn} and b_{mn}^2 were obtained by adding $S_{mn}^{\beta(k)}(\mathbf{r})$ and $S_{mn}^{b^2(k)}(\mathbf{r})$ according to (see ref. [27])

$$I_{mn}^{\beta}(\mathbf{r}) = \frac{1}{M}\sum_{k=1}^{M} S_{mn}^{\beta(k)}(\mathbf{r}) \tag{4a}$$

$$I_{mn}^{b^2}(\mathbf{r}) = \frac{1}{M}\sum_{k=1}^{M} S_{mn}^{b^2(k)}(\mathbf{r}) \tag{4b}$$

Consequently, by applying this nonlinear image processing technique defined by Eq. (4), a maximum value of the nonlinear coefficients was achieved at the defect location $\mathbf{r} = \mathbf{r}_d$.

III. Linear Ultrasonic Imaging Methods

Literature provides a quantitative number of diagnostic LUIM that can provide a detailed image of the structural damage. In this Section, five LUIM imaging techniques are reported as a benchmark for NEWT to retrieve the corrosion defect on an aluminium panel using sparse sensor arrays. These include time of arrival, time difference of arrival, energy arrival, reconstruction algorithm for the probabilistic inspection of damage (RAPID) and Rayleigh maximum-likelihood estimate (RMLE). Although these methodologies have been individually reported for different types of damages, to the authors' knowledge, an overall comparison with NUIM is still missing. Unlike nonlinear sensing methods, LUIM require additional signal processing as they rely on the residual waveforms, $r_{mn}[\theta]$, which are the differences between the received signals, $f_{mn}[\theta]$, containing the damage information (as seen in the previous Section), and the

baseline ones, $s_{mn}[\theta]$, i.e. the waveforms associated to the undamaged structure recorded from each transmitter-receiver pair. The envelope-detected signals $h_{mn}[\theta]$ are calculated from the residual signals $r_{mn}[\theta]$ and their Hilbert transform as follows:

$$h_{mn}[\theta] = |r_{mn}[\theta] + jH(r_{mn}[\theta])|, \tag{5}$$

where $H(r_{mn}[\theta])$ is the Hilbert transform of $r_{mn}[\theta]$.

III.1 Time of Arrival or Ellipse Method

The Ellipse method is a delay-and-sum beamforming applied to an exponential windowed form, $h_{mn}^{(w)}[\theta]$, of the envelope-detected signals $h_{mn}[\theta]$ according to [3]

$$h_{mn}^{(w)}[\theta] = h_{mn}[\theta] e^{\frac{(\theta - \zeta'_{mn})}{\alpha f_s}} \tag{6}$$

where ζ'_{mn} is the index corresponding to the arrival time of the direct waveform between each transmitter-receiver pair, and α and f_s are a decay coefficient and the sampling frequency, respectively. In our experiments, α was chosen equal to 77.8 μs, (corresponding to a propagation distance of 400 mm) as this value resulted in the highest performance in terms of localisation error. Once $h_{mn}^{(w)}[\theta]$ is calculated for all transducers pair combinations, the 2D imaging map, $I_{mn}^{TOA}(\mathbf{r})$, in the ellipse method can be obtained according to

$$I_{mn}^{TOA}(\mathbf{r}) = \sum_{m=1}^{N} \sum_{n=m+1}^{M} h_{mn}^{(w)}[\zeta_{mn}(\mathbf{r})], \tag{7}$$

where $\zeta_{mn}(\mathbf{r})$ is the direct time of flight index, i.e. the index corresponding to the time that the waveforms take to travel from the transmitter location to any point, $\mathbf{r}$, of the aluminium panel and the receiver location. It should be pointed out that calculation of

$\zeta_{mn}(\mathbf{r})$ requires the knowledge of group velocity of the propagating elastic waves. For a single transducers pair, Eq. (7) maps the elastic wave propagation into the medium as an ellipse with its foci set at the transmitter-receiver locations. Hence, as additional pairs are added, the ellipses intersect at the damage location.

III.2 Time Difference of Arrival or Hyperbola Method

This imaging method is based on the assumption that the windowed enveloped detected signals, $h_{mn}^{(w)}[\theta]$ and $h_{mp}^{(w)}[\theta]$, actuated by the *m*th same transmitting sensor and measured at two receiver transducers *n* and *p*, are correlated according to the time difference from a given region to each of the receiver sensors [4]. If a damage is present at location $\mathbf{r} = \mathbf{r}_d$, its reflections will appear in the recorded waveforms with different time delays, and the cross correlation $C_{mn,mp}[\theta]$ between the two windowed enveloped detected signals will give a maximum at the damage location. Based on these considerations, the 2D intensity map, $I_{mn}^{TDOA}(\mathbf{r})$, for the hyperbola method is given by

$$I_{mn}^{TDOA}(\mathbf{r}) = \sum_{m=1}^{M} \sum_{\substack{n=1 \\ n \neq m}}^{N} \sum_{\substack{p=n+1 \\ p \neq m}}^{M} C_{mn,np}[\Delta\zeta_{mn}(\mathbf{r})], \tag{8}$$

where $\Delta\zeta(\mathbf{r})$ is the index corresponding to the time difference that the propagating waveforms would take to travel from the transmitting source to a given point **r** on the panel and then to each of the two locations of receiver transducers. From Eq. (8), the correlation function corresponds to a set of hyperbolas that cross the location of the defect with the foci at the two receivers' location.

III.3 Energy Arrival Method

The energy arrival method is an adaptively version of the ellipse imaging method, which rely on a weighted form of the elastic wave energy function [5]. In this technique, the residual signals, $r_{mn}[\theta]$, are windowed about the calculated arrival time index, $\zeta_{mn}(\mathbf{r})$, and the 2D image, $I_{mn}^{EA}(\mathbf{r})$, can be obtained as

$$I_{mn}^{EA}(\mathbf{r}) = \sum_{m=1}^{N} \sum_{n=m+1}^{M} \frac{E_{mn}^{win} - E_{mn}^{cum}}{E_{mn}^{win} + E_{mn}^{cum}}, \tag{9}$$

where:

$$E_{mn}^{cum} = \sum_{\theta=1}^{\zeta_{mn}} r_{mn}^2[\theta], \quad E_{mn}^{win} = \sum_{\theta=\zeta_{mn}}^{\zeta_{mn}+\tau} r_{mn}^2[\theta], \tag{10}$$

with τ the index of the time history corresponding to the time window starting at $\zeta_{mn}(\mathbf{r})$, and E_{mn}^{cum} and E_{mn}^{win} the cumulative and window energies, respectively. During the tests, the time window τ was chosen to 15 μs. The inversion of the wave energy in Eq. (9) adaptively reduces the amplitude of the scattered waveforms.

III.4 Reconstruction Algorithm for the Probabilistic Inspection Damage Method

The Reconstruction Algorithm for the Probabilistic Inspection Damage (RAPID) imaging method is based on the statistical correlation coefficient, $\Phi_{mn}[\theta]$, which is a measure of the strength of the expectation value between the damaged signals, $f_{mn}[\theta]$, and the undamaged ones, $s_{mn}[\theta]$, each with sample size Ξ [6]. If $f_{mn}[\theta]$ and $s_{mn}[\theta]$ are uncorrelated, $\Phi_{mn}[\theta]$ is zero, whilst if the damaged and baseline waveforms are correlated in some way, the statistical correlation coefficient is nonzero. Analogously to the ellipse method, 2D images $I_{mn}^{RAPID}(\mathbf{r})$ are generated by spatially distributing $\Phi_{mn}[\theta]$

for each signal difference into an elliptical pattern with the foci being at the transmitter-receivers' location as follows:

$$I_{mn}^{RAPID}(\mathbf{r}) = \sum_{m=1}^{N}\sum_{n=m+1}^{M}\left(1-\Phi_{mn}[\theta]\right)\left[\frac{\beta - R_{mn}(\mathbf{r})}{\beta - 1}\right], \tag{11}$$

where β is a parameter that control the size of the elliptical pattern (in our experiments β was set equal to 1.2) and:

$$R_{mn}(\mathbf{r}) = \begin{cases} \zeta_{mn}(\mathbf{r})/\zeta'_{mn}, & if\ \beta > \zeta_{mn}(\mathbf{r})/\zeta'_{mn} \\ \beta, & otherwise \end{cases}. \tag{12}$$

III.5 Rayleigh Maximum Likelihood Estimate Method

The Rayleigh Maximum Likelihood Estimate (RMLE) method is based on the principle of maximum likelihood of the envelope-detected signals $h_{mn}[\theta]$ [7]. The likelihood function L is the probability density function of the Rayleigh distribution, D, of the envelope-detected signals, $h_{mn}[\theta]$, and corresponds to the probability of observing a given data set as functions of $h_{mn}[\theta]$ and the Rayleigh parameters, $\sigma_{mn}^{dir}[\zeta_{mn}(\mathbf{r})]$ and $\sigma_{mn}^{scat}[\zeta_{mn}(\mathbf{r})]$. These last two terms are the standard deviations of the envelope-detected signals before and after the direct time of flight index $\zeta_{mn}(\mathbf{r})$, respectively. Since the observed data set are the coordinates $\mathbf{r}$ on the plane of the aluminium panel, the likelihood function simplifies to (the time index θ is omitted for clarity reasons):

$$L(\mathbf{r}, \sigma_{mn}^{dir}, \sigma_{mn}^{scat} | h_{mn}) = \prod_{mn} D(\mathbf{r}, \sigma_{mn}^{dir}, \sigma_{mn}^{scat} | h_{mn}), \tag{13}$$

with

$$D(\mathbf{r}, \sigma_{mn}, | h_{mn}) = \frac{h_{mn}[\theta]}{\sigma_{mn}^2[\zeta_{mn}(\mathbf{r})]} \exp\left(-\frac{h_{mn}^2[\theta]}{2\sigma_{mn}^2[\zeta_{mn}(\mathbf{r})]}\right). \tag{14}$$

Rather than determining the maximum of the product of Eq. (13), the logarithm of the likelihood function is calculated, which leads to the 2D map $I_{mn}^{RMLE}(\mathbf{r})$ as follows:

$$I_{mn}^{RMLE}(\mathbf{r}) = \sum_{mn} \log D\left(\mathbf{r}, \sigma_{mn}^{dir}, \sigma_{mn}^{scat} \middle| h_{mn}\right). \quad (15)$$

As the maximum likelihood estimation makes the observed data set most probable for the envelope-detected signals $h_{mn}[\theta]$, the coordinates of the damage location $\mathbf{r}_d$ are obtained as the maximum values of $I_{mn}^{RMLE}(\mathbf{r})$.

IV. Experimental Set-up

For the experimental set-up, a 2024 aluminium panel with dimensions of 600 x 600 x 5 mm was used and eight piezoelectric sensors (maximum seven receivers at a time) were surface bonded over its top surface (Fig.1). Each transducer was used as transmitter whilst the others served as receivers allowing the creation of the 2D images as reported in the previous Section. Sensors and damage coordinates are reported in Table 1.

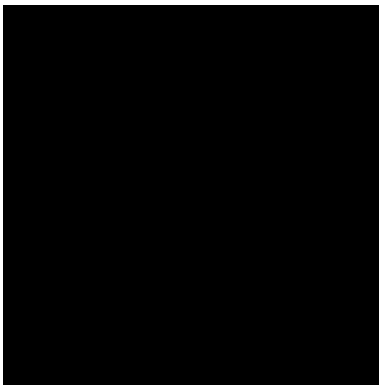

Figure 1 Illustration of the tested aluminium panel with the sensors configuration and damage location.

Table 1 Sensors and damage coordinates

	x-coordinate (mm)	**y-coordinate (mm)**
Sensor 1	180	520
Sensor 2	320	520
Sensor 3	480	520
Sensor 4	480	300
Sensor 5	480	120

Sensor 6	320	120
Sensor 7	180	120
Sensor 8	180	300
Damage (corrosion)	250	190

The transmitter sensors were linked to a preamplifier and connected to a National Instrument (NI) data acquisition system consisting of the NI PXI 5421 16-bit arbitrary waveform generator card to send a 5-cycles Hanning-windowed tone burst at 200 kHz. Such a fundamental frequency was tuned to find the local maxima in the second order nonlinear structural response after a swept signal ranged between 150 and 250 kHz, thus to fulfil the QPC condition. This can be clearly seen in Fig. (2), which illustrates the maximum of the bicoherence b_{mn}^2 [Eq. (2)] achieved at $f_1 = 200$ kHz.

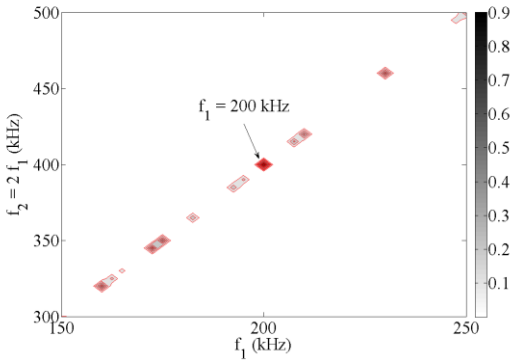

Figure 2 Bicoherence measured from of one of the receiver transducers.

Figure 3 shows the presence of the second harmonic response at 400 kHz in the spectrum of the measured signal from one the receiver sensors due to the interaction of the elastic waves with the corrosion damage.

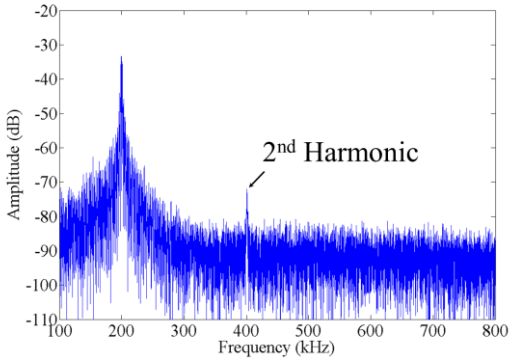

Figure 3 Spectrum of the measured signal from one of the receiver sensors

The piezoelectric transducers (APC sensors) with diameter of 6.35 mm and thickness of 2.5 mm were designed to excite and measure the fundamental symmetric Lamb mode S_0. At the chosen excitation frequency, the group velocity of the propagating guided mode S_0 is 5142 m/s with a wavelength of nearly 25 mm. Figure 4 reports the dispersion curves of the fundamental and first Lamb modes for an aluminium structure with a thickness of 5 mm. In addition, the applied voltage was around 150 V in order to maximise the efficiency of the available sensors.

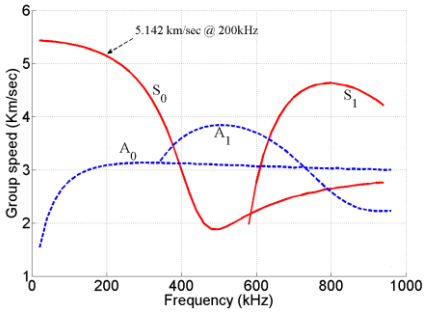

Figure 4 Dispersion curves for an aluminium plate with thickness of 5 mm.

For the execution of LUIM, the undamaged sample was first tested to record the library of baseline signals $s_{mn}[\theta]$. The waveforms, acquired at ambient temperature (around 20°C), were averaged twenty times to reduce the Gaussian noise. Each structural response was sampled at 20 MHz with a total acquisition time of 6 msec to account for signal reverberations from the defect location. Corrosion damage was then introduced

through a controlled material degradation process and finally the imaging algorithms were performed. It should be noted that the damaged waveforms, $f_{mn}[\theta]$, were measured at the same environmental and operational conditions of the baseline signals (the maximum temperature variation was $\pm 3.5\,°C$). Hence, this research work did not require any optimal baseline subtraction methods to compensate temperature effects on the acquired signals [29], [30]. Figure 5 illustrates the time histories of the normalised residual signals (continuous blue colour lines) measured by the seven receiver transducers and the associated envelope detected waveforms (dashed red colour lines).

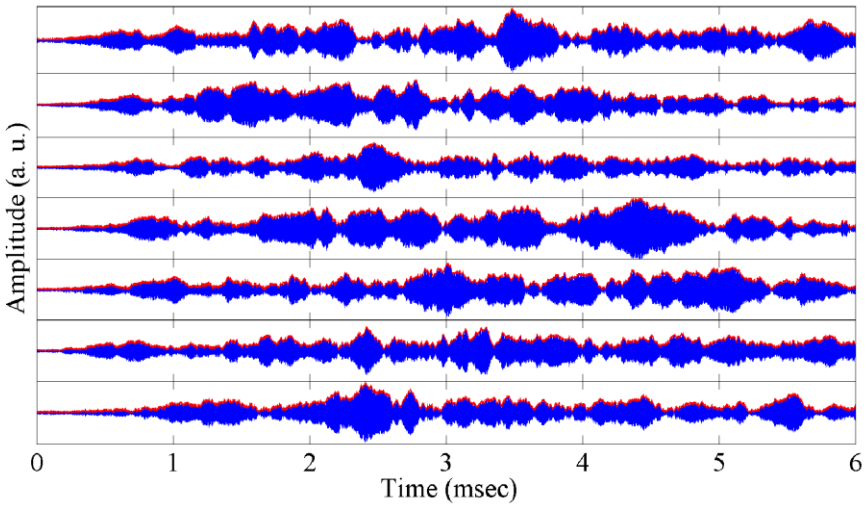

Figure 5 Residual signals, i.e. the differences between the received signals containing the damage information and the baseline ones (continuous blue line), and their envelopes (dashed red line). The amplitude of residual signals was normalised between 0 and 1.

IV.1 The Corrosion Process

After the application of a Teflon mask on the top surface of the aluminium panel, a small region of interest (10 x 10 mm) was subjected to two different corrosion processes. The first one involved HNO_3 concentrated (Sigma-Aldrich 70%, density of 1.413 g/ml at 20°C). A uniform layer of HNO_3 was deposited using a glass pipette [31]. After three hours, 2 g of bicarbonate was used to neutralise the acid environment and

distilled water was used to clean the surface. A change of colour was noticed as a proof of the action of the acid on the first layer of aluminium oxide that covers the surface of the aluminium panel. The second process was aimed at accelerating the corrosion action of the acid over the top surface. According to Ghali [32], this technique consisted of an attack with H_2SO_4 concentrated (Sigma-Aldrich, ACS reagent 95 - 98%, density of 1.840 g/ml at 20°C) along the region of interest. After twenty hours, the attack with H_2SO_4 was strong enough to corrode the surface enchanting a localised corrosion. The final crack was measured at about 4 mm due to some forms of localised attack, i.e. pits or crevices. This appeared to be straight with branches near the top end. According to Solodov et al. [33], the second order nonlinear behaviour can be attributed either to the "clapping" motion of the region normal to the damage interface or to the nonlinear friction between the defect surfaces, which are excited by small tangential stresses produced by the elastic waves propagating through the medium.

V. Imaging Results

In order to obtain a final 2D improved image of the damage, simple addition of the images from different transducers pairs was performed with NEWT [Eq. (4)], whilst the minimum pixel value method was adopted as image fusion strategy for LUIM [3]. According to Section II, the 2D maps of the damage location with both linear and nonlinear techniques using eight sensors are represented in Figure 6. The imaging results of each technique were shown in linear colour scale and each image was normalised by the maximum amplitude value of the pixel. The dark black colour corresponds to the maximum peak intensity, whilst the white colour is zero. In all the

figures, the white circles are the transducers location, whereas the black square and circle are the true and estimated damage locations, respectively.

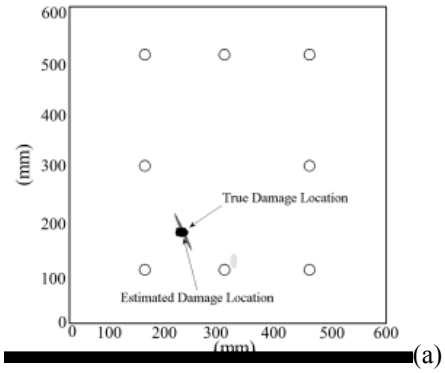

(a)

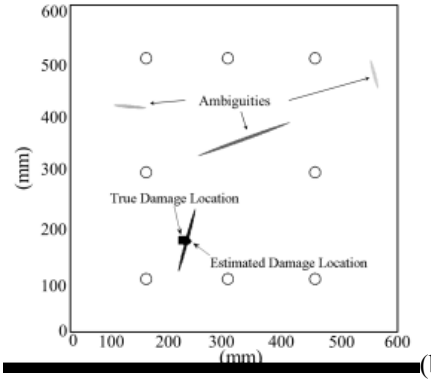

(b)

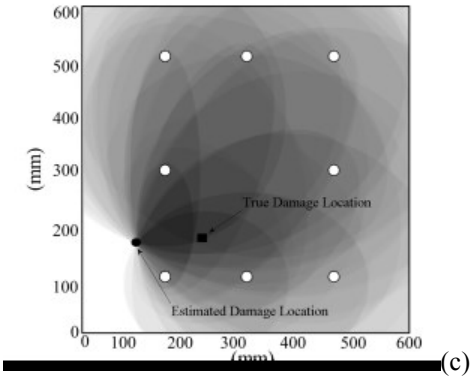

(c)

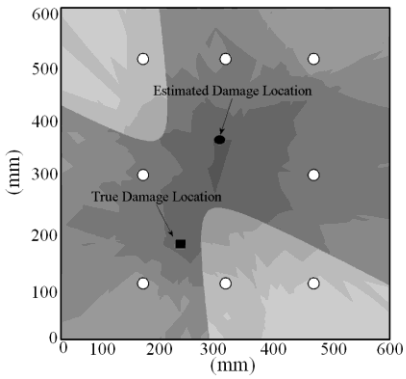

(d)

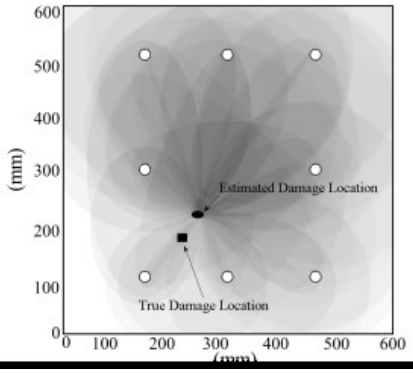

(e)

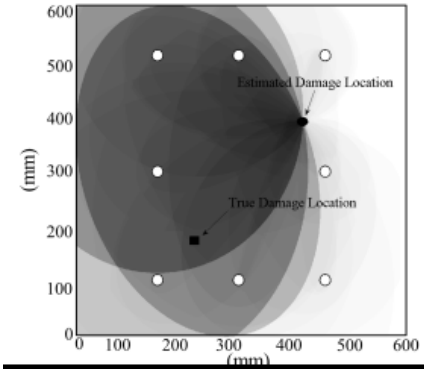

(f)

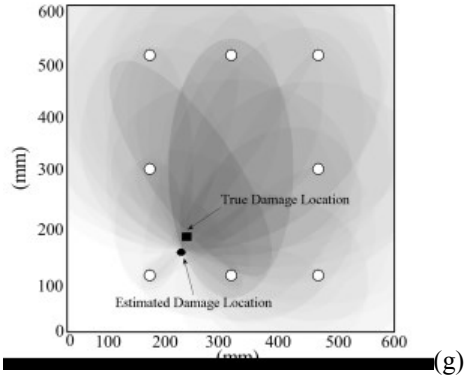

(g)

Figure 6 NEWT and LUIM for damage location using eight transducers. Bicoherence and RBF method (a), second order nonlinear coefficient and RBF method (b), ellipse method (c), hyperbola method (d), energy arrval method (e), RAPID method (f) and RMLE method (g).

Among LUIM, the most accurate prediction was achieved using the RMLE method. Indeed, according to the error function ψ defined as $\psi = |\mathbf{r}_d - \mathbf{r}_{de}|$ where $\mathbf{r}_{de} = x_{de}\hat{i} + y_{de}\hat{j}$ is the position vector of the estimated damage location, a maximum error of $\psi = 25$ mm was found using the RMLE technique. Moreover, Figure 6 showed that a combination of bicoherence parameter and RBF allowed achieving a perfect identification of the defect corrosion location, with an error function equal to zero. Similar results were obtained by reducing the number of transducers to six and four elements [Figs. (7) and (8)].

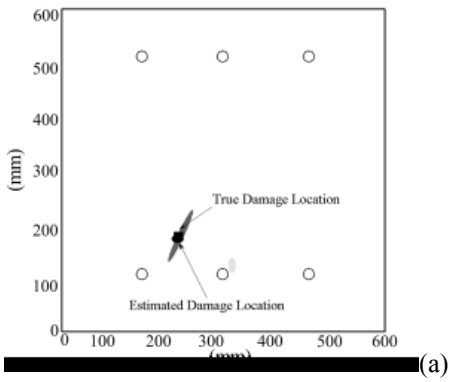

(a)

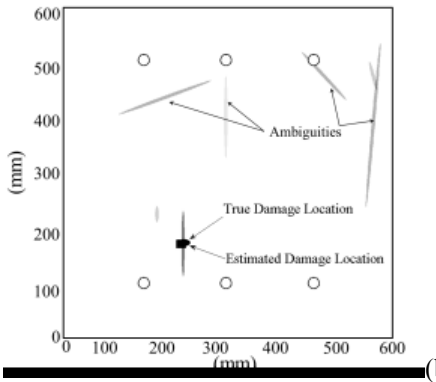

(b)

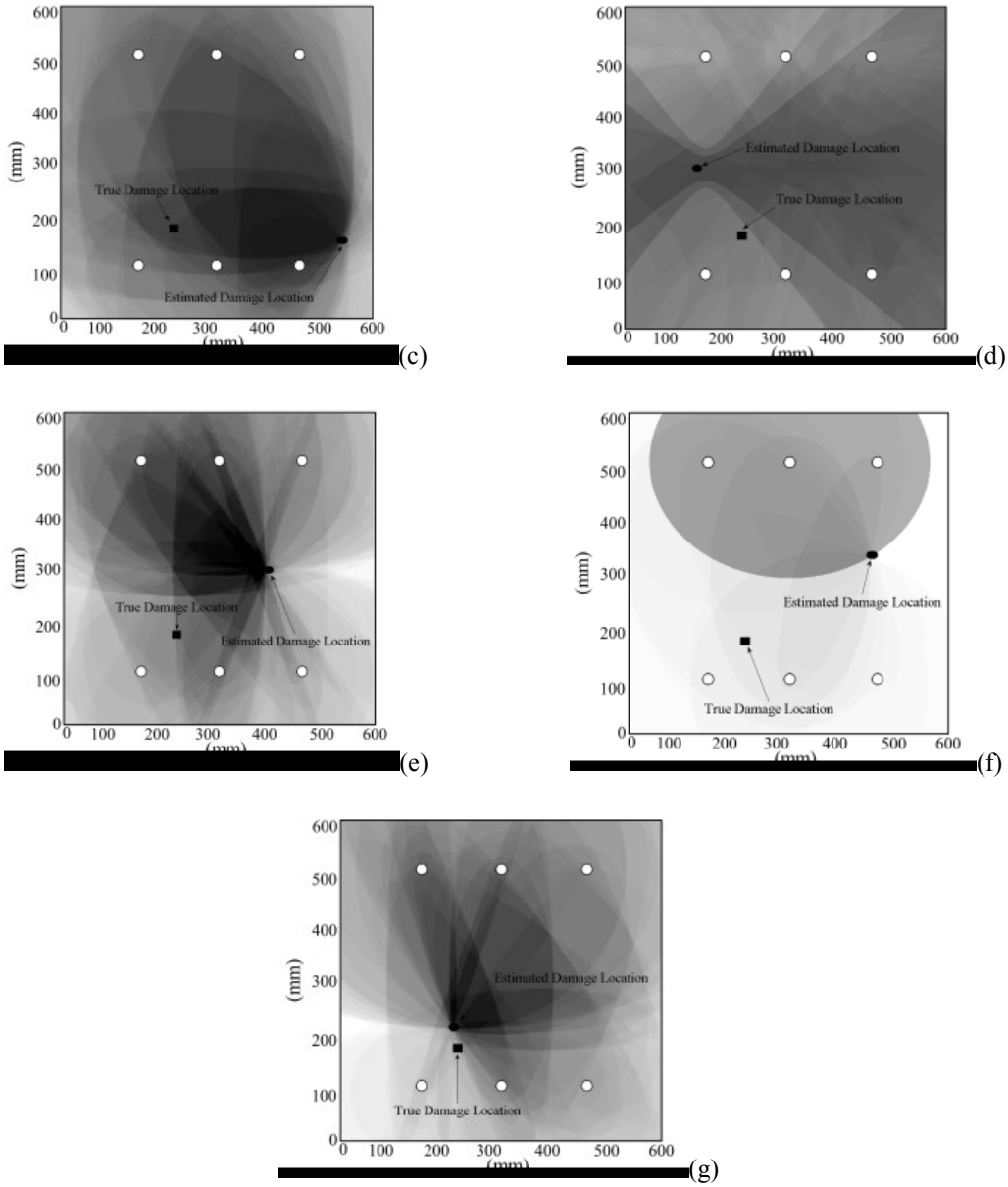

Figure 7 NEWT and LUIM for damage location using six transducers. Bicoherence and RBF method (a), second order nonlinear coefficient and RBF method (b), ellipse method (c), hyperbola method (d), energy arrval method (e), RAPID method (f) and RMLE method (g).

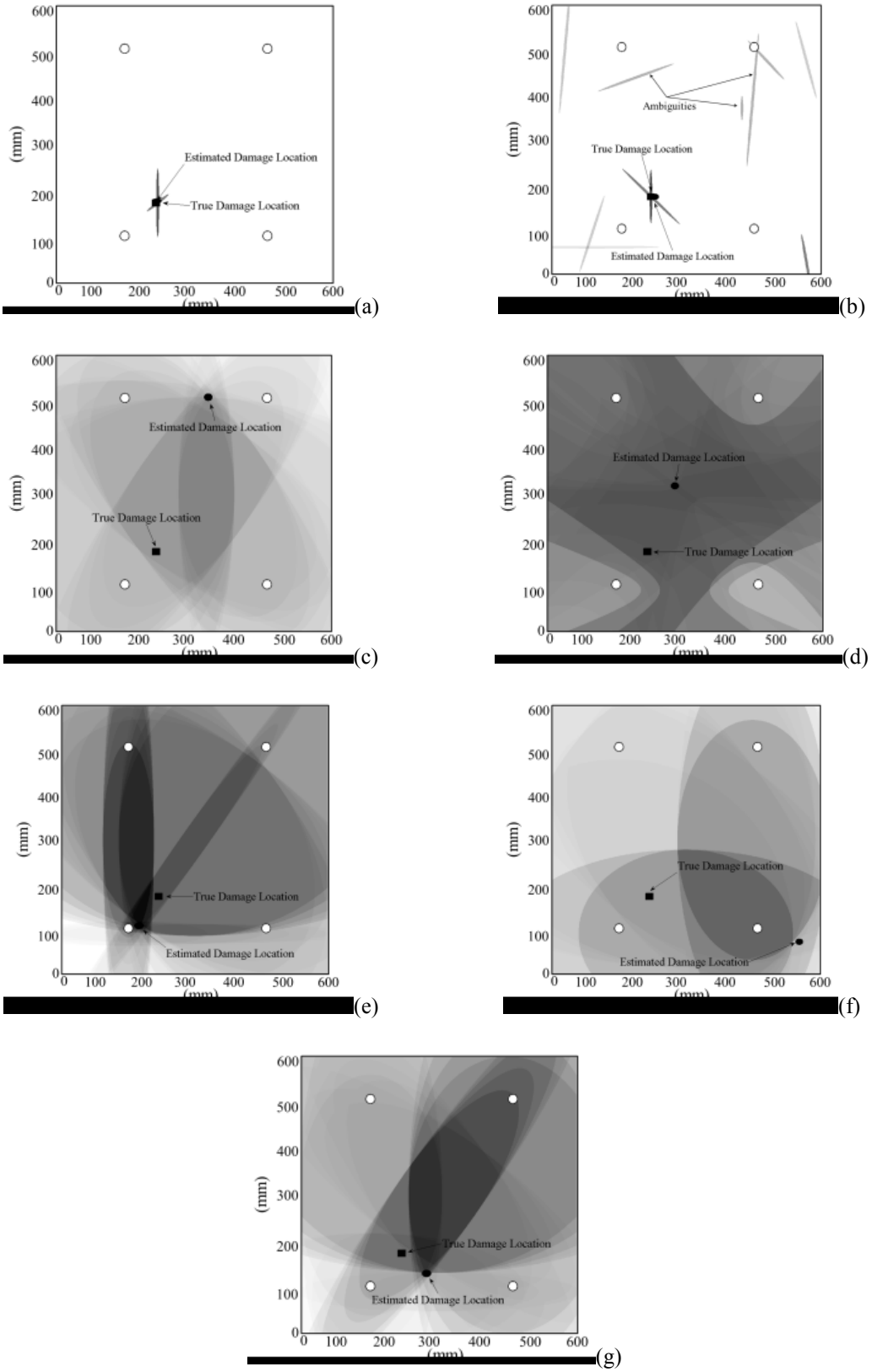

Figure 8 NEWT and LUIM for damage location using four transducers. Bicoherence and RBF method (a), second order nonlinear coefficient and RBF method (b), ellipse method (c), hyperbola method (d), energy arrval method (e), RAPID method (f) and RMLE method (g).

Table 2 reports the damage coordinates and the error function for both linear and nonlinear imaging methods.

Table 2 Damage coordinates and error function for both LUIM and NEWT.

	x-coordinate (mm)	y-coordinate (mm)	Error Function ψ (mm)
TOA – 8 Sensors	120	185	poor localisation
EA – 8 Sensors	270	225	40
TDOA – 8 Sensors	310	365	poor localisation
RAPID – 8 Sensors	430	400	poor localisation
RMLE – 8 Sensors	230	175	25
β + RBF – 8 Sensors	251	190	no error + ambiguities
b^2 + RBF – 8 Sensors	250	290	no error
TOA –6 Sensors	550	170	poor localisation
EA – 6 Sensors	410	300	poor localisation
TDOA – 6 Sensors	170	300	poor localisation
RAPID – 6 Sensors	475	345	poor localisation
RMLE – 6 Sensors	245	220	30
β + RBF – 6 Sensors	252	191	no error + ambiguities
b^2 + RBF – 6 Sensors	250	290	no error
TOA –4 Sensors	360	520	poor localisation
EA – 4 Sensors	190	125	88
TDOA – 4 Sensors	300	320	poor localisation
RAPID – 4 Sensors	560	90	poor localisation
RMLE – 4 Sensors	300	150	64
β + RBF – 4 Sensors	251	190	no error + ambiguities
b^2 + RBF – 4 Sensors	250	290	no error

Interestingly, the EA method was the only imaging technique that performed better with eight and four sensors but not with six elements. Indeed, such a technique is the only approach that takes into account the scattered and reflected waves in the localisation process. Similar results were found also in [7]. Moreover, although the numbers of sensors was drastically reduced up to only four elements, NEWT still maintained high performance in retrieving the damage location. Finally, from Figures 6-8 it can be seen that unlike bicoherence, the nonlinear sensing method with the standard second order nonlinear parameter β did not provide a perfect damage localisation, as image ambiguities were present over the surface of the panel [Figures (6-8b)]. Such detrimental artefacts were due to the spurious experimental source of nonlinearity such as the amplifier due to the high input amplitude, or the coupling between the sensor and

the aluminium structure. Indeed, as the parameter β does not preserve any information of the phase of the measured signals, the quadratic phase coupling between the fundamental and the second harmonic frequencies is inevitably lost [25]. However, our studies demonstrated that NEWT measurements based on bicoherence and RBF can be used as a useful tool for monitoring the presence of corrosion damages using a sparse array of receiver sensors. Further studies will be aimed at investigating how multiple corrosion defects and their evolution over time will affect the linear and nonlinear ultrasonic response of propagating waves.

VI. Conclusions

This paper presented a nonlinear elastic wave tomography method, based on ultrasonic guided waves, for the image of the corrosion damage in isotropic structures. The proposed methodology relies on a combination of higher order statistic such as bispectral analysis and radial basis function interpolation to obtain a two-dimensional spatial map of the defect using a reduced number of sparse sensors arrays. In particular, the bicoherence parameter was used to characterise the second order nonlinear signature contained in the measured signals due to the presence of the structural defect. The performance of this nonlinear sensing technique was compared with that of five linear imaging methods. The experimental results showed the effectiveness of the nonlinear tomography sensing technique for structural health monitoring applications as it allowed achieving a perfect localisation of the damage.

References

[1] W. J.-N. de Lima and M.-F. Hamilton, "Finite-amplitude waves in isotropic elastic plates", J. Sound Vib. **265**, 819 (2003).

[2] G. Scarselli, A. Maffezzoli, E. Castorini, A. Taurino, "Vibrational analysis of aerospace composite components for production defects and operating damage detection", *Proceedings of 9th International Conference on Composite Science and Technology (ICCST9)*, 811-819, (2013).

[3] . J.-E. Michaels, T.-E. Michaels, "Guided wave signal processing and image fusion for in situ damage localization in plates", *Wave Motion*, 44, 482-492, (2007).

[4] A. Croxford, P. Wilcox, B., Drinkwater, G. Konstantinidis, "Strategies for guided-wave structural health monitoring", *Proc. R. Soc. A*, 463, 2961-2981 (doi:10.1098/rspa.2007.0048), (2007).

[5] J.-E. Michaels, T.-E. Michaels, "Damage Localization in Inhomogeneous Plates Using a Sparse Array of Ultrasonic Transducers", *AIP Conference Proceedings*, 894, 846-853, (2007).

[6] H. Gao, Y. Shi, J. Rose, "Guided wave tomography on an aircraft wing with leave in place sensors", *AIP Conf. Proc.*, 760, 1788-1794 (doi:10.1063/1.1916887), (2005).

[7] E. Flynn, M.-D. Todd, P.-D. Wilcox, B.-W. Drinkwater, A. Croxford, "Maximum Likelihood estimation of damage location in guided-wave structural health monitoring", *Proc. R. Soc. A*, 467 2575–96, (2011).

[8] F., Ciampa, E., Barbieri, M. Meo, "Modelling of multiscale nonlinear interaction of elastic waves with three dimensional cracks", *J. Acoust. Soc. Am*. ***135*** *(4)*, 3209, (2014).

[9] F., Ciampa, E., Onder, E., Barbieri, M. Meo, "Detection and Modelling on Nonlinear Elastic Response in Damaged Composite Structures", *J. Nondestr. Eval.* ***33***, *515*, (2014)

[10] O. Bou Matar, P.-Y Guerder, Y. Li, B. Vandewoestyne, K. E.-A. Van Den Abeele. "A nodal discontinuous Galerkin finite element method for nonlinear elastic wave propagation". *J. Acoust. Soc. Am*. ***131*** (*5*), pp. 3650-63 (2012)

[11] M. Meo, G. Zumpano, "Nonlinear elastic wave spectroscopy identification of impact damage on a sandwich plate", *Composite Structures*, 71: 469–474, (2005).

[12] K. E.-A. Van Den Abeele, P.-A. Johnston, A. Sutin. "Nonlinear elastic wave spectroscopy (NEWS) techniques to discern material damage, part I: nonlinear wave modulation spectroscopy (NWMS)". *Res. Nondestr. Eval.* ***12*** (*1*), 17-30 (2000).

[13] G., Zumpano, M., Meo, "Damage localization using transient non-linear elasticwave spectroscopy on composite structures", *International Journal of Non-Linear Mechanics*, **43**: 217 – 230, (2008).

[14] P.-B. Nagy, L. Adler. "Acoustic Nonlinearity in plastics", in Review of Progress in Quantitative Nondestructive Evaluation, edited by D. O. Thompson and D. E. Chimenti (Plenum, New York, 1992), Vol. **I IB**, 2025-2032, (1992).

[15] F. Ciampa, M. Meo, "Nonlinear elastic imaging using reciprocal time reversal and third order symmetry analysis", *J. Acoust. Soc. Am.* **131**, pp. 4316–4323 (2012).

[16] F. Ciampa, S. Pickering, G. Scarselli, M. Meo, "Nonlinear damage detection in composite structures using bispectral analysis", *Proc. SPIE. 9064, Health Monitoring of Structural and Biological Systems 906402 (9 March 2014);* doi: 10.1117/12.2046631, (2014).

[17] L., Ostrovsky, P.-A., Johnson, “Dynamic nonlinear elasticity in geomaterials,” Riv. Nuovo Cim. **24**, 1−46, (2001).

[18] K. E.-A. Van Den Abeele, A., Sutin, J., Carmeliet, P. A., Johnson, “Micro-damage diagnostics using nonlinear elastic wave spectroscopy (news),” *NDT&E. Int.* **34**:239–48, (2001).

[19] F. Amerini, M., Meo, “Structural health monitoring of bolted joints using linear and nonlinear acoustic/ultrasound methods”, *Structural Health Monitoring - An International Journal,* **10** (6), pp. 659-672, (2011).

[20] J., Kyung-Young, “Applications of Nonlinear Ultrasonics to the NDE of Material Degradation”. *IEEE transactions on ultrasonics, ferroelectrics, and frequency control*, 47(3):540-8, (2000).

[21] Y.-C. Kim, E.-J. Powers, “Digital Bispectral Analysis and its Applications to Nonlinear Wave Interactions,” *IEEE Transactions on Plasma Science,* Ps-7, 120-131, (1979).

[22] V., Zaitsev, V., Nazarov, V., Gusev, B., Castagnede, “Novel nonlinear-modulation acoustic technique for crack detection”, *NDT & E Int.* **39**, 184–194, (2006).

[23] L. D. Landau, E. M. Lifshitz, [Theory of Elasticity], Chap. III, *Pergamon*, Oxford, (1986).

[24] C.-L., Nikias, M.-R., Raghuveer, “Bispectrum estimation: a digital signal processing framework,” *Proc. IEEE* **75**, 869-91 (1987).

[25] J. W.-A., Fackrell, S., McLaughlin, “The Higher Order Statistics of Speech Signals,” Proceedings of the IEE Colloquium on Techniques in Speech Signal Processing, London, Digest No. 1994/138, 7/1-7/6 (1994).

[26] J. W.-A., Fackrell, P.-R.,White, J.-K., Hammond, R.-J., Pinnington, and A.-T., Parsons, “The interpretation of the bispectra of vibration signals - I. Theory”, *Mechanical System and Signal Processing* **9**(3), 257–266, (1995).

[27] F. Ciampa, S. Pickering, G. Scarselli, M. Meo, “Nonlinear imaging of damage in composite structures using sparse ultrasonic sensor arrays”, Journal submitted to *Structural Health Monitoring - An International Journal,* (2014)

[28] de Boer, A. van der Schoot, M.-S., Bijl, H. “Mesh deformation based on radial basis function interpolation”, Comput Struct, **85** (11–14), pp. 784–795, (2007).

[29] T Clarke, F Simonetti and P Cawley, “Guided wave health monitoring of complex structures by sparse array systems: Influence of temperature changes on performance”, J. Sound Vib. **329** 2306–22 (2010).

[30] F. Ciampa, S. Boccardi, M. Meo, “Factors affecting the imaging of the impact location with inverse filtering and diffuse wave fields”, Journal submitted to *Structural Health Monitoring - An International Journal,* (2014).

[31] J.R. Davis (Ed.), ASM specialty handbook: aluminum and aluminum alloys, ASM International, Metals Park (OH) (1993).

[32] E. Ghali, R.W. Revie, Corrosion Resistance of Aluminum and Magnesium Alloys (first ed) John Wiley & Sons, Hoboken, New Jersey (2010)

[33] I. Solodov, N. Krohn, G. Busse, CAN: an example of nonclassical acoustic nonlinearity in solids, *Ultrasonics **40***, 621–625, (2002).